Structural and Multidisciplinary Optimization (2019) 59:1935–1947
https://doi.org/10.1007/s00158-018-2164-3

RESEARCH PAPER

A multi-objective optimization framework for robust axial compressor airfoil design

Ivo Martin[1] · **Lennard Hartwig**[1] · **Dieter Bestle**[1]

Received: 22 February 2018 / Revised: 7 November 2018 / Accepted: 22 November 2018 / Published online: 4 January 2019

Abstract
Airfoil design for stationary gas turbines is a challenging task involving both aerodynamic and structural aspects. The paper describes a multidisciplinary optimization process for axial compressor airfoils which is able to find optimal designs w.r.t. multiple objectives and constraints starting from a reference design and very few specifications of the new compressor. The process allows to simultaneously execute arbitrarily many instances of design evaluation processes independently from each other, which speeds it up, not just due to parallelization, but also because fast-running low-fidelity evaluation may take the design lead at an early design stage, whereas high-fidelity evaluation processes simultaneously contribute with more reliable results on the actual performance. For consistency of aerodynamic and structural analysis, an innovative method for direct loaded-to-unloaded design transformation is incorporated. Additionally, the process accounts for design robustness by utilizing production tolerances as an optimization objective. Therefore, a procedure is developed which allows to find the production tolerance which may be allowed without violating any constraints. An application example demonstrates that the proposed optimization process incorporating automatic detection of failure-critical eigenmode bands is able to shift them such that structurally reliable, robust, and simultaneously aerodynamically efficient designs are obtained.

Keywords Multidisciplinary design optimization · Robustness · Production tolerance assessment · Loaded-to-unloaded transformation · Structural analysis · Aerodynamic analysis

1 Introduction

The design of airfoils has to take into account multiple aerodynamic and structural constraints, where design improvements have to balance multiple contradictory objectives. Therefore, the development process is expensive w.r.t. both time and computational resources, which led to increasing efforts in developing multi-objective, multidisciplinary, and multi-fidelity optimization processes during the last two decades. Although the complexity of such processes has continuously increased, there is still potential for improvement w.r.t. speed, design quality, and flexibility. For example, Diener et al. (2016) or Pierret et al. (2007) execute aerodynamic and structural design evaluations successively where one discipline has to wait for the other to finish. Such kind of process is ineffective due to idling of those analysis parts which are currently not in action. This also concerns the work of Buske et al. (2016) who executed several slave processes in parallel, where again complete computational fluid dynamics (CFD) and finite element analyses (FEA) are performed in sequential order. The effectiveness of such serial approaches is harmed in two ways: first, licenses are not fully exploited due to idle time of waiting subprocesses, and second, inclusion of time-consuming evaluation tools from some disciplines may degrade the performance of other algorithms. In contrast to this, the process proposed here is able to run an arbitrary number of instances of different evaluation processes simultaneously by coupling them through response surface models (RSMs) as suggested by Hartwig and Bestle (2016). This allows different processes to run at their own speed without slowing down others.

Another issue of many of the latest multidisciplinary airfoil design processes is the absence of loaded-to-unloaded transformation. In consequence, the results of aerodynamic and structural assessment may not be consistent in regards to the underlying design geometry.

Responsible Editor: Mehmet Polat Saka

✉ Ivo Martin
Ivo.Martin@b-tu.de; ivo@martin-erkner.de

[1] BTU Cottbus-Senftenberg, Cottbus, Germany

Astrua et al. (2012) and Joly et al. (2014) assume that differences between structural results based on loaded or unloaded geometry would be negligible. However, the results in this paper prove different which is in agreement with the understanding of Buske et al. (2016), who use an iterative loaded-to-unloaded transformation method described by Goerke et al. (2012). This method being industrial standard is, however, considerably time consuming. Therefore, an alternative approach is suggested here which is much faster and easier to implement, because it is directly incorporated into the FE analysis.

One of the key components in practical optimization is design evaluation w.r.t. robustness, because without this the obtained designs are likely to be located at the boundaries of the design space set by design constraints. This may cause many produced parts to violate constraints due to uncertainties in manufacturing and operating conditions. Production tolerances may also deteriorate the performance (objectives) to such an extent that other nominal designs being less sensitive may outperform deterministically found optimal designs on average. In the past, many authors have developed design processes incorporating design robustness w.r.t. objectives by simultaneously minimizing their mean value and variance such as Motta and Afonso (2016) or Flassig et al. (2008), who consider robustness w.r.t. constraints via a failure rate. Although Dow and Wang (2015) assess production tolerances as a more constructive measure than the failure rate, considerations are only qualitative. All these approaches lack a clear measure which can be communicated to suppliers in order to ensure design robustness during production. For this reason, the present paper introduces a strategy for assessing that production tolerance which just avoids violation of constraints as an additional objective. This tolerance is supposed to be maximized in order to minimize production costs.

The content of this paper will primarily focus on the structural design evaluation part of the coupled structural-aerodynamic process, which implements methods suggested by Martin and Bestle (2016) and Martin and Bestle (2018) in order to identify failure-critical eigenmode shapes and assign corresponding eigenfrequency bands bounded by upper and lower uncertainty limits. Due to this feature and the correlation between eigenmode shape and risk of failure, the proposed process is capable of risk-specific eigenfrequency tuning in order to avoid harmful resonances in forced responses. To the authors' best knowledge, this is unique and the only comparable process was reported by Blocher and Fernández (2014) where risk of forced response and failure is assessed via the prediction of stress levels using time consuming, unsteady, coupled flow-structure analyses for all relevant operating and installation conditions.

The first part of the paper will explain the general structure of the underlying optimization process. The second part shares details about the parameter model, while the third part describes the optimization problem with details on objectives and constraints. Further, new methods of robust design evaluation by assessing production tolerances and the loaded-to-unloaded transformation strategy are introduced. Finally, optimization results are generated and discussed.

2 Optimization process

The foundation of compressor design process presented here has been developed over 15 years in close cooperation with an aero engine manufacturer and adapted to the specific features of stationary gas turbines within the project mentioned in the acknowledgments at the end of the paper. It accounts for industrial needs identified in intensive discussions and is supposed to deliver robust designs (for annulus and airfoils) based on a reference design and some new design targets discussed within this paper. The final design shall be most efficient w.r.t. aerodynamics, have maximum reliability by ensuring structural integrity and reducing the risk of critical forced response, and minimize production costs by maximizing manufacturing tolerances. In the first phase of the design process in Fig. 1a.

The geometry of the annulus, the segmentation of stages, and the number of blades/vanes per stage are determined in a meanline-based optimization process (Keskin 2007) coupled with a throughflow-based process, Rühle and Bestle (2010) and Pöhlmann and Bestle (2012). In order to meet the pressure and temperature requirements gained from the combined meanline-throughflow optimization, a first guess of the airfoil geometries is calculated by the knowledge-based autoblading process superposing airfoil profiles on multiple 2D stream tubes as defined by Wu (1952) and Cumpsty (2004). The design parameter model presented in Section 3 is fitted to this initial airfoil to set proper bounds for the subsequent blading process to search for optimal designs within these bounds.

The present paper focused on the second phase of the compressor design which is the blading in Fig. 1b. During this blade optimization, the 3D compressor blades will be evaluated simultaneously by a low-fidelity quasi-2D aerodynamic code (approx. 10-s CPU time), a high-fidelity 3D RANS CFD (approx. 8 h) and FEM analysis (approx. 30 min). Due to the different runtimes of the three disciplines, in a classic optimization process with sequential design evaluation, the faster processes would be idling most of the time while the slow 3D RANS calculation is carried out. Therefore, the maximum number of design assessments to solve optimization problem using a classic optimization process is limited

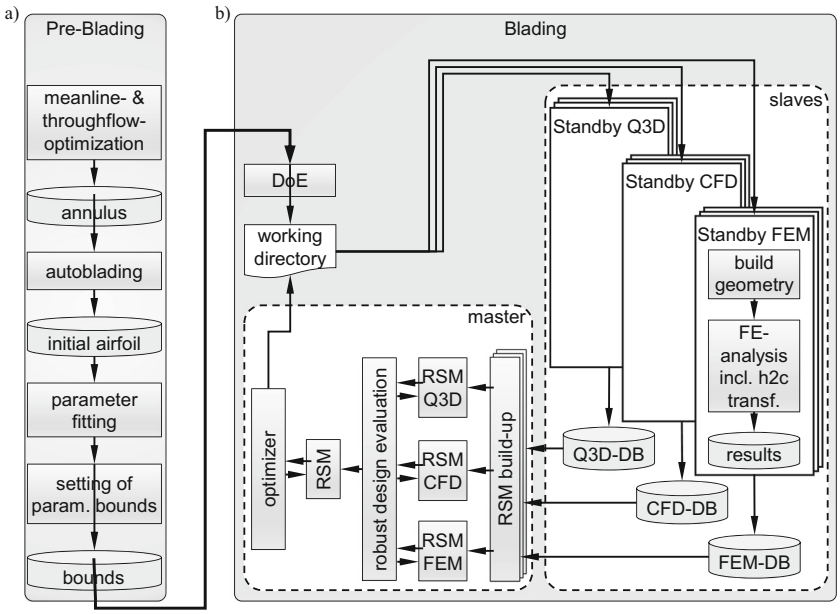

Fig. 1 Pre-blading process **(a)** and multidisciplinary blade optimization process **(b)**

by the slowest subprocess (3D RANS), even when using parallelization and simultaneous evaluation of several designs. To overcome these limitations, a surrogate-based optimization process has been developed as described in Hartwig and Bestle (2016), which decouples design evaluation by the three disciplines from each other and also from the optimization, where a genetic algorithm (GA) explores the design space by proposing promising designs, based on excessive exploration of the response surfaces built-up in the involved disciplines.

To be more precise, the blade optimization in Fig. 1b starts with an initial design of experiments (DoE) where the samples are written into a working directory. From there, they can be picked up individually by independent standby slave processes for design evaluation, which are multiple instances of analysis processes referring to different and/or equivalent disciplines. The corresponding results are generated at a discipline-dependent, individual speed and written to discipline-specific databases (DB). Because of the simultaneous execution of different disciplines (each with a different number of instances due to different runtime), the specific databases may not necessarily contain results for the same set of designs taken from the working directory. Thus, individual response surface models (RSMs) have to be built up by the master process from the actually available design points in the data bases and associated results.

The optimizer then searches for new designs based on these RSMs only as suggested by Hartwig and Bestle (2016) who showed such an approach find optimal solutions faster due to the ability to decouple processes and subsystems. A multi-objective genetic algorithm (MOGA) has been chosen for this task, since it is capable of solving complex multi objective problems, and even more important, is able to overcoming local minima. It may be worthwhile to mention that even a single discipline, e.g., CFD, may deliver several RSMs depending on the number of associated objectives and constraints. Here, RSMs are generated using PLS-Kriging as described by Hartwig and Bestle (2017) which reduces design space dimension by combining Kriging with partial least squares in order to identify the principle components of the response behavior. Response surfaces are then only generated w.r.t. these most-influencing design parameters.

Since accuracy of the RSMs built from the designs generated by the initial DoE is low, the process in Fig. 1b iteratively suggests new designs in two ways simultaneously. First, it is a space-filling algorithm (distance maximization to previously evaluated design points) to uncover possibly new regions of local minima and to improve accuracy of the surrogate models globally. Second, samples from the Pareto front of optimal designs with respect to the actual optimization objectives (objective minimization and constraint fulfillment) are selected to improve RSM accuracy locally. New designs are written to the common working directory and continuously picked up by the slave processes to be evaluated. The evaluated results are stored in the corresponding databases and an RSM update will be triggered including the new designs. The RSM-based optimization will then be carried out again using the improved surrogate models until the resulting Pareto front does not change significantly anymore.

Writing the results into discipline-specific databases offers a superior way of parallelization where instead of executing, e.g., CFD and FEA in series on multiple CPUs (central processing unit), arbitrary and nonconforming

numbers of CFD and FEA may run in parallel. The advantage is that despite the scaling capacity of the solver, not only the calculations are parallelized, but also pre- and post-processing. Here, three parallel FEA processes evaluating three different designs simultaneously, each using only a single CPU, are able to process more samples from the working directory per hour than a single FEA process running on 20 CPUs. Additionally, not only less CPUs are required, but also fewer licenses. In case all designs in the working directory have been analyzed, the slaves idle in standby until new designs are written to the working directory. This happens especially for the fast-running quasi-3D (Q3D) evaluation process w.r.t. aerodynamics, whereas specific picking strategies had to be developed for the long-running CFD and FEA processes to balance local and global search, see Hartwig and Bestle (2016).

3 Geometry and design parameterization

The geometry model is based on Dutta (2011) where airfoil profiles are defined on 21 sections and the spaces in between are interpolated by using piecewise cubic splines. Each section is defined on a x-$r\theta$-stream-surface, Fig. 2, identified by normalized average radius

$$\tilde{r} = \frac{\bar{r} - \bar{r}^{Hub}}{\bar{r}^{Tip} - \bar{r}^{Hub}}, \tag{1}$$

where $\bar{r} = (r_L + r_T)/2$ results from streamline radii r_L and r_T at the leading and trailing edge, respectively, which are both obtained from the meanline-throughflow process. The section geometry within each section layer is defined by superposing the dimensionless thickness distribution

$$\tilde{t}(\tilde{r}, \tilde{c}) = \left\{ \begin{array}{l} \frac{t(\tilde{r},\tilde{c}) - R_L(\tilde{r})}{t_{max}(\tilde{r}) - R_L(\tilde{r})} \text{ for } 0 \le \tilde{c} \le c^*(\tilde{r}) \\ \frac{t(\tilde{r},\tilde{c}) - R_T(\tilde{r})}{t_{max}(\tilde{r}) - R_T(\tilde{r})} \text{ for } c^*(\tilde{r}) < \tilde{c} \le 1 \end{array} \right\} \tag{2}$$

with the dimensionless camber-line-angle distribution

$$\tilde{\beta}(\tilde{r}, \tilde{c}) = \frac{\beta(\tilde{r}, \tilde{c}) - \beta_L(\tilde{r})}{\beta_T(\tilde{r}) - \beta_L(\tilde{r})}. \tag{3}$$

They are determined by describing the leading- and trailing-edge radius distributions $R_L(\tilde{r})$ and $R_T(\tilde{r})$, the maximum-thickness distribution $t_{max}(\tilde{r})$, inlet and outlet blade angle distributions $\beta_L(\tilde{r})$ and $\beta_T(\tilde{r})$, and normalized chord coordinate $\tilde{c} \in [0, 1]$. The fillet of the airfoil is defined through a fillet radius R_F and the connection height h_F, where both are limited by the blade height H. Furthermore, lean and tilt can be applied via the parameters' theta-shift $\theta_S(\tilde{r})$ and axial-shift $\tilde{x}_S(\tilde{r})$, respectively.

The tip clearance is no optimization parameter and must be pre-selected for the loaded geometry, because the parametrized designs are hot geometries fully loaded at design speed and will be transformed to the actual respective unloaded cold geometry before structural assessment. The tip clearance is created by extrapolation of the airfoil beyond the tip, followed by a cut off at a defined distance from the casing. The airfoil root is currently also not part of the optimization process, but pre-defined. Alternatively, it may be received from an optimization, as described by Schörner and Bestle (2012), and incorporated into the structural evaluation process.

For optimization, the distribution functions in Fig. 2b depending on $\tilde{r}$ and $\tilde{x}$ have to be replaced by discrete design parameters. Therefore, the radial distributions of t_{max}, θ_S, and $\tilde{x}_S$ are represented by cubic Bézier-splines as shown in Fig. 3a, and the radial distributions of R_L, R_T, β_L, and β_T are parameterized with quadratic Bézier-splines. The camber angle $\tilde{\beta}(\tilde{r}, \tilde{c})$ is represented by a Bézier-spline surface of quadratic order in $\tilde{r}$-direction and cubic order in $\tilde{c}$-direction (Fig. 3b), and $\tilde{t}(\tilde{r}, \tilde{c})$ is represented by a piecewise quadratic B-spline surface (Fig. 3c). Since the root of the airfoil shall not be shifted by axial- and theta-shift modifications, the first control point of $\tilde{x}_S(\tilde{r})$ and $\theta_S(\tilde{r})$ is fixed at position [0, 0], respectively. Additionally, the control points of $\tilde{\beta}$ and $\tilde{t}$ with the same grid position in $\tilde{r}$-direction are shifted simultaneously, which reduces the number of design parameters without influencing the design freedom of the spline surfaces too much. According to the degrees of freedom (DoF) of each control point (in Fig. 3: line ≡ 1 DoF, rectangle ≡ 2 DoF, cube ≡ 3 DoF) and the parameters for the fillet definition $\tilde{R}_F = R_F/H$ and

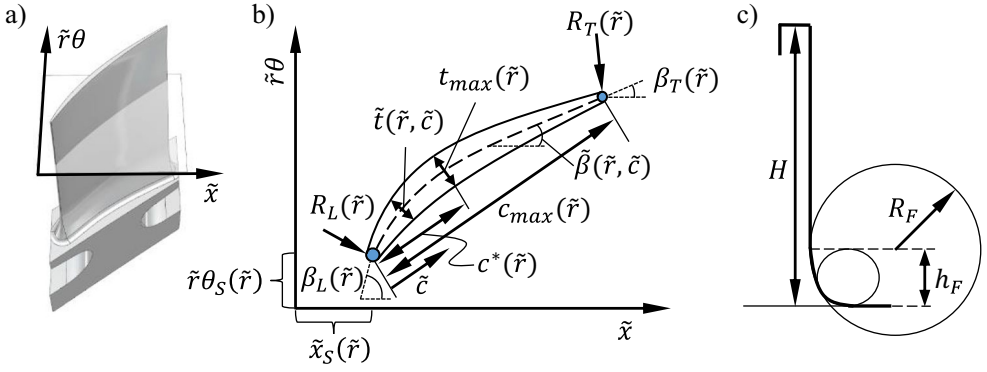

Fig. 2 Geometry model with **a** section plane, **b** section parameterization, and **c** fillet model on a schematic representation of an airfoil with height H

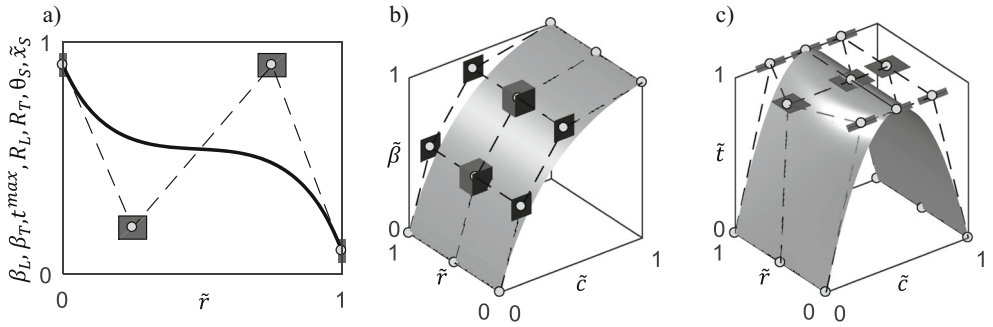

Fig. 3 Bézier- and B-spline representation of **a** geometry parameters with only radial dependence, **b** camber-line angle, and **c** thickness distribution

$\tilde{h}_F = h_F/R_F$, see Fig. 2c, the total number of design parameters is $N_P = 57$. In order to restrict the change of spline control points, upper $(\hat{p}_i)$ and lower $(\check{p}_i)$ bounds are set for each optimization parameter p_i as indicated by box sizes in Fig. 3. The initial setting of the control points referring to an existing reference blade or a design derived from AutoBlading is received by spline-fitting, see Fig. 1a.

4 Robust design problem

The optimization of an airfoil design has to account for multiple objectives f_i to be minimized and inequality constraints $h_i \leq 0$. In the following, the focus will be on the relevant structural objectives and constraints; aerodynamic constraints such as proper flow turning or bounds on Mach number will not be explained any further and may be found, e.g., in Dutta (2011). Thereafter, the consideration of design robustness within the optimization problem will be explained.

4.1 Structural constraints

In order to ensure structural integrity and producibility of the optimized designs, several constraints have to be taken into account by the optimization process and therefore assessed by using FEA (details on the utilized FE model are described by Martin and Bestle 2016). For example, minimum life may be guaranteed by limiting the overall maximum von Mises stress σ^{max} by the minimum strain limit $R_{p02}(T_{max})$ occurring at the maximum possible temperature T_{max} during operating conditions, i.e., $\sigma^{max}/R_{p02} - \alpha_{p02} \leq 0$, where $0 < \alpha_{p02} < 1$ is a safety factor. The risk of crack initiation is limited by analogously enforcing that the maximal von Mises stresses at the leading edge σ_L^{max} and trailing edge σ_T^{max} are bounded by $\hat{\sigma} = \alpha_{p02} R_{p02}(T_{max})$ as $\sigma_L^{max} - \hat{\sigma} \leq 0$ and $\sigma_T^{max} - \hat{\sigma} \leq 0$.

The lifetime of airfoil designs may be maximized by minimizing the risk of high-cycle fatigue (HCF). Therefore, as a first criterion the alternating von Mises stresses $\sigma_{a,i}$ of the i^{th} eigenmode calculated with the finite element method (FEM) shall not exceed the endurance limit $\sigma_a^*(\sigma_{m,i})$ which can be identified from the Haigh diagram (Nicholas 2006) by using the mean von Mises stress $\sigma_{m,i}$ of the i^{th} eigenmode assessed with FEM. The definition of an upper limit L_a to the alternating stress ratio yields the following constraints for the first eleven eigenmodes:

$$\frac{\sigma_{a,i}}{\sigma_a^*(\sigma_{m,i})} - L_a \leq 0\ ,\ i = 1, 2, ..., 11. \tag{4}$$

Additionally, the risk of forced eigenmode excitation by engine orders within the working-speed range of the compressor should be minimized. However, uncertainties in operating conditions, e.g., in temperature and fixation conditions of the airfoils, make it impossible to predict eigenfrequencies f_i^E accurately resulting in eigenfrequency bands between an upper limit $\hat{f}_i^E$ and a lower limit $\check{f}_i^E$. These limits can be calculated from the extrema in operating and installation conditions. For hammer-foot roots, the extrema are no contact to neighboring airfoil roots at hot and full contact at cold conditions, Hecker et al. (2011). Risk of resonance due to forced vibration may then be assessed by an intersection measure $0 \leq Int_{ij} \leq 1$ of the intersection between eigenfrequency bands $\left[\check{f}_i^E, \hat{f}_i^E\right]$ and engine orders $f_j^A = nN_j$ ($n \hat{=}$ engine speed [rpm]; $N_j \hat{=}$ number of installations) within the working-speed range $[\check{n}_{ij}, \hat{n}_{ij}]$ as introduced by Martin and Bestle (2016), where a value of zero means no intersection within speed range and one means full intersection. Since risk of failure also correlates with the eigenmode shape due to the location of stress concentrations, intersections may be penalized individually by factors $w_i^E \geq 0$ associated with eigenmode type and $w_j^A \geq 0$ accounting for the strength of the source of excitation. The final forced response criterion, called mode-resonance factor, then reads as

$$MRF_i := \sum_j Int_{ij} \left(w_j^A + w_i^E\right). \tag{5}$$

Intersection-free designs require $MRF_i = 0$, which may be also expressed by an inequality constraint $MRF_i \leq 0$; else $MRF_i > 0$ correlates with the risk of forced response

vibrations. In order to assign correct penalty factors, Martin and Bestle (2018) developed methods for mode-shape classification based on neural networks. The cornerstone is the ability to compare displacement fields of different airfoil geometries by projecting them onto an uniform standard using Kohonen maps (self-organizing neural networks), Martin and Bestle (2016).

Not only forced response, but also self-induced excitation, i.e., flutter, is relevant for HCF. Therefore, four more generic criteria are applied. The first two define a lower limit $\breve{F}_i$ on the Strouhal-number St (Strouhal 1878) describing the frequency of eddy shedding in the Kármán-vortex street, i.e.,

$$\breve{F}_i - \frac{2\pi\, c_{max} \mid_{\tilde{r}=0.75} \breve{f}_i^E \mid_{n\hat{=}100\%}}{w_1 \mid_{\tilde{r}=0.75}} \leq 0\ ,\ i = 1, 2, \tag{6}$$

where $c_{max} \mid_{\tilde{r}=0.75}$ and $w_1 \mid_{\tilde{r}=0.75}$ are the chord length and relative speed of attack at 75% blade height, respectively, and $\breve{f}_i^E \mid_{n\hat{=}100\%}$ is the lower limit of the first and second eigenfrequency at 100% engine speed. The other two criteria are experience based and classified by the industrial partner of the research project.

In order to ensure that found airfoil designs can be manufactured, the leading- and trailing-edge radii $R_{L/T} \geq \breve{R}$ are bounded by a minimum producible radius $\breve{R}$. The radii are additionally limited by $R_{L/T} \geq \alpha t_{max}$, $0 < \alpha < 1$, in order to reduce risk of crack initiation due to erosion by requiring a minimal thickness. Both constraints may be summarized as

$$R_{L/T} \geq \max\left\{\breve{R}, \alpha t_{max}\right\}. \tag{7}$$

Because of the dependence on maximum blade thickness t_{max} and the rather indirect control of the $R_{L/T}\,(\tilde{r})$-distribution via spline control points, these distributions are calculated first in the design process and then immediately analyzed whether they violate the constraints (7) or not. If a distribution fails this check, the corresponding design would not be analyzed by slave processes, but a high penalty value of 9999 is assigned to all objectives and constraints.

4.2 Robust design objectives

As the design space $P \subset \mathbb{R}^{N_P}$ is limited by several inequality constraints $h_i\,(\mathbf{p}) \leq 0$ mentioned above, optimal designs are likely to be located at the borders of the constrained design space where some $h_i = 0$, Flassig (2011). Consequently, parameter uncertainties w.r.t. such a nominal design, e.g., due to production variances, will result in a large number of parts to fail the constraints and also deteriorate the predicted performance. In order to minimize design sensitivity to production variances, design robustness must be part of the optimization problem. In the following, the maximum possible production tolerance for a nominal design $\mathbf{p}^{nom}$ will be introduced as a suitable robustness objective.

Typically, the robustness of a nominal design $\mathbf{p}^{nom}$ w.r.t. constraints is described by the failure rate, i.e., the percentage of designs in a set of samples $\mathcal{D} := \left\{\mathbf{p}_1^{\Delta}, ..., \mathbf{p}_{N_S}^{\Delta}\right\}$ of N_S random points in the neighborhood $(\mathbf{p}^{nom} \pm \Delta\mathbf{p})$ of $\mathbf{p}^{nom}$ failing at least one constraint $h_i \leq 0$. However, the failure rate is a rather problematic robustness measure as the examples in Fig. 4a demonstrates. Let the gray boxes be infeasible design regions A and B where at least one constraint fails. Then the sample causes the same failure rate in both cases, but obviously the parameter tolerances Δp_2^A and Δp_2^B, within which variations do not fail at all, are totally different. 3A more practical approach for robust design assessment, however, should not even analyze such tolerances in the design space, but analyze if real geometry variations within a specific production tolerance $\pm s_{\perp}$ violate any constraints, see Fig. 4b. In case no constraints are violated, $\mathbf{p}^{nom}$ may considered to be robust within the specific tolerance $\pm s_{\perp}$. Hence, the goal should not be to minimize the failure rate, but to maximize the largest possible production tolerance. While using failure rate as a robustness measure is justified for mass-produced parts with little overall profit losses in case of failure, the maximum possible production tolerance is the only valid requirement to suppliers of expensive and safety-critical parts. Its computation does not require any assumption on probabilistic parameter distributions, since any part produced within this tolerance must be valid. Hence, applying uniform distributions to the parameter variations is sufficient.

Actually, sampling and assessing only geometry variations within a defined production tolerance may be difficult because of the complex shape of that region $\mathcal{P}$ in the design space P, which is associated with all possible geometry variations of the nominal design $S\,(\mathbf{p}^{nom})$ within the tolerance band $\Omega\,(\mathbf{p}^{nom}, s_{\perp})$, see gray regions in Fig. 4b, c. In order to identify a subset $\mathcal{P} \subseteq \mathcal{D}$ of designs $\mathbf{p}_j^{\Delta}$, the associated shape $S\left(\mathbf{p}_j^{\Delta}\right)$ (white curve in Fig. 4b) is generated as a CAD model (computer-aided design) and checked, if it lies within the tolerance band $\Omega\,(\mathbf{p}^{nom}, s_{\perp})$ (gray band in Fig. 4b) of the nominal shape $S\,(\mathbf{p}^{nom})$ (black curve in Fig. 4b). Only for these sample points $\mathbf{p}_j^{\Delta} \in \mathcal{P}$ constraint violation is checked.

The goal is to find the maximal possible production tolerance $\pm s_{\perp}^{max}$, where disturbed designs $\mathbf{p}_j^{\Delta} \in \mathcal{P}$ do not violate any further constraint than the nominal design $\mathbf{p}^{nom}$. This may be achieved with the following iterative procedure:

1. Define $s_{\perp} := \Delta s_{\perp}$ as the minimal feasible tolerance step that can be manufactured, e.g., $\Delta s_{\perp} = 0.01$mm.

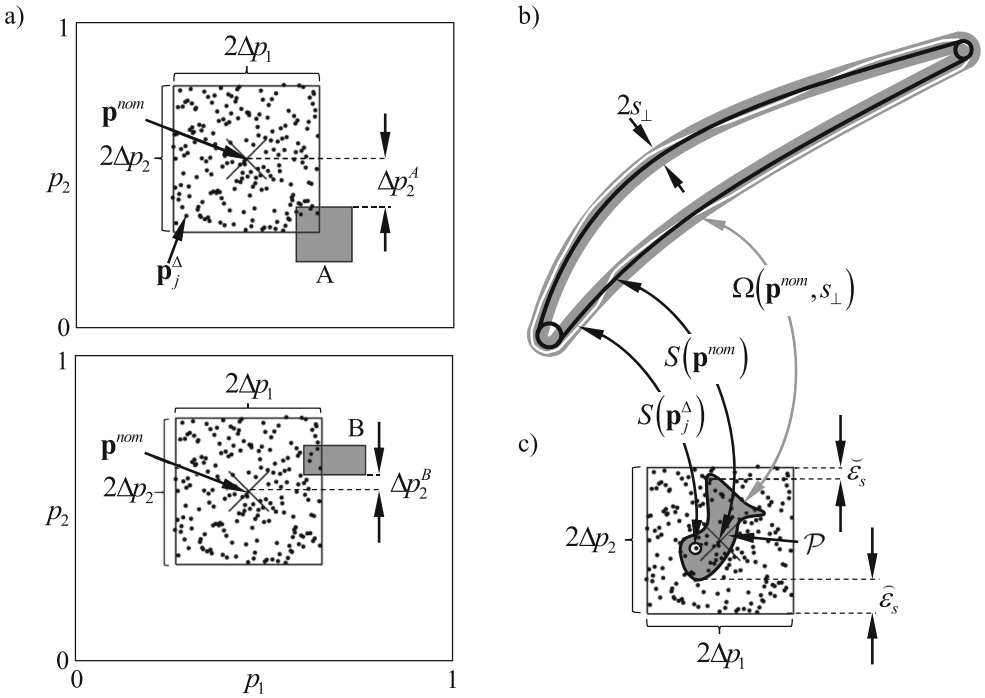

Fig. 4 Robustness assessment with a) failure rate and b) production tolerance $\pm s_\perp$

2. Create a sample $\mathcal{D}$ of design points within a sufficiently large range ($\mathbf{p}_{nom} \pm \Delta\mathbf{p}$).
3. From all designs $\mathbf{p}_j^{\Delta} \in \mathcal{D}$, identify those where the associated airfoil shape is contained in the tolerance hull, i.e., $S\left(\mathbf{p}_j^{\Delta}\right) \in \Omega\left(\mathbf{p}^{nom}, s_\perp\right)$, in order to receive a design subset $\mathcal{P}$ being feasible w.r.t. the actual value of production tolerance $s_\perp$.
4. Calculate the number of variations $\mathbf{p}_j^{\Delta} \in \mathcal{P}$ that violate additional constraints compared to $\mathbf{p}^{nom}$, i.e.,

$$\Delta N_V\left(\mathbf{p}^{nom}, s_\perp\right) := \left|\left\{\mathbf{p}_j^{\Delta} \in \mathcal{P} \,\middle|\, \exists i : h_i\left(\mathbf{p}^{nom}\right) \leq 0 \wedge h_i\left(\mathbf{p}_j^{\Delta}\right) > 0\right\}\right|. \quad (8)$$

5. In case $\Delta N_V\left(\mathbf{p}^{nom}, s_\perp\right) = 0$, increase tolerance as $s_\perp := s_\perp + \Delta s_\perp$ and continue from step 2; else maximum tolerance $s_\perp^{max} = s_\perp - \Delta s_\perp$ is obtained.

In order to minimize the risk of incomplete sampling in step 2, the minimum distance of any $\mathbf{p}_j^{\Delta} \in \mathcal{P}$ from the borders of the sampling neighborhood should be at least some user-defined lower gap value $\breve{\varepsilon}_S$, see Fig. 4c; else $\pm\Delta\mathbf{p}$ has to be adapted. Equivalently, in order to keep the sampling density reasonably high, the closest sample points $\mathbf{p}_j^{\Delta} \in \mathcal{P}$ to each of the sampling borders should have a distance below some user-defined upper gap value $\hat{\varepsilon}_S$. Due to the adaption of the gaps $\breve{\varepsilon}_S$ and $\hat{\varepsilon}_S$ in each iteration step, the method here does not rely on arbitrarily chosen sampling ranges for the parameters in contrast to the commonly applied failure rate.

The calculated tolerance $s_\perp^{max}$ presents a valuable criterion for design robustness; however, it will not be incorporated directly because of its discrete nature ($s_\perp^{max} = k\Delta s_\perp, k \in \mathbb{N}$). In order to smooth the measure, it is assumed that the failure rate within the set of samples $\mathcal{P}$ for the next, but non-robust tolerance step $s_\perp^{max} + \Delta s_\perp$, is a measure of how much of this non-robust tolerance step might be possible. The assumption is reasonable, because the failure rate of the design variations within the assessed tolerance $\pm s_\perp^{max}$ is zero. Therefore, the failure rate

$$F_R := \frac{\Delta N_V\left(\mathbf{p}^{nom}, s_\perp^{max} + \Delta s_\perp\right)}{|\mathcal{P}|} \quad (9)$$

is calculated and a continuous minimization objective for maximizing the production tolerance is defined as

$$\tilde{s}_\perp^{max} := -\left(s_\perp^{max} + (1 - F_R)\,\Delta s_\perp\right). \quad (10)$$

4.3 Formulation of the optimization problem

Typical design objectives for compressor blade design are the pressure loss Δp_t at design-point operation conditions as well as off-design losses ω_{OD}. In the presence of manufacturing uncertainties, their influence has to be considered in a probabilistic manner which is typically done by minimizing mean and variance of each objective, since smaller variance is associated with lower sensitivity to design variations, Flassig (2011). Such a split of each deterministic objective into two equivalent robust design criteria, however, harms the optimization performance by doubling the number of objectives. Therefore, they are here combined to 95%-percentiles P_*^{95}, Du et al. (2004), which define a specific objective value where 95% of the

observations result in lower values. As a statistical measure, their computation requires a relevant sample size to be evaluated within a defined parameter range $\pm\Delta\mathbf{p}$ about each nominal design $\mathbf{p}^{nom}$. For comparability, the sampling range $\Delta\mathbf{p}$ has to be the same for all nominal designs. With the percentile and the production tolerance (10) the final robust optimization problem reads as

$$\min_{\mathbf{p}^{nom}\in P} \begin{bmatrix} P^{95}_{\Delta p_t} \\ P^{95}_{\omega_{OD}} \\ \tilde{s}^{max}_{\perp} \end{bmatrix} \quad \text{s.t.}$$

$$P := \left\{ \mathbf{p}^{nom} \in \mathbb{R}^{N_P} \,\middle|\, \begin{bmatrix} \mathbf{h}^{\text{Aero}} \\ \mathbf{h}^{\text{FEM}} \end{bmatrix} \leq \mathbf{0} \;,\; \check{\mathbf{p}} \leq \mathbf{p}^{nom} \leq \hat{\mathbf{p}} \right\} \;, \tag{11}$$

where all aerodynamic and structural constraints mentioned above are summarized in vectors $\mathbf{h}^{\text{Aero}}$ and $\mathbf{h}^{\text{FEM}}$, respectively.

5 Loaded-to-unloaded transformation

Design optimization is typically based on a parameterization of the loaded geometry during regular operating conditions inducing airfoil deformations due to centrifugal and pressure loads as well as high-temperature deformations. However, in order to correctly determine associated stress, strain, eigenfrequencies, and eigenmodes, the finite element analysis has to start from the unloaded configuration at room temperature conditions. In order to ensure consistency between loaded and unloaded geometries during the combined aerodynamic and structural design optimization (11), a proper loaded-to-unloaded transformation has to be performed, where the unloaded geometry has to be determined such that, after applying nominal loads and temperatures, the geometry will deform to the original loaded geometry. The often used current approach described by Goerke et al. (2012) aims at finding the unloaded geometry iteratively as follows:

1. Starting with the known loaded geometry L_0 in Fig. 5a, assume unloaded geometry $U_1 \equiv L_0$ to be identical as a first guess; set $i = 1$.
2. Apply the load and temperature conditions to U_i resulting in a corresponding loaded geometry L_i.
3. Subtract the difference $\Delta_i := L_i - U_i$ from the desired loaded geometry L_0 to obtain a better guess U_{i+1} of the unloaded geometry.
4. Set $i := i + 1$ and proceed with steps 2 and 3 until absolute error $|L_i - L_0| \leq \varepsilon$ is below an user-defined tolerance ε; finally U_i is the desired estimate of the unloaded geometry associated with H_0.

This iterative procedure accounts for nonlinearities due to the stepwise nonlinear FE analyses, but is rather time consuming due to the stepwise extraction of displacements from FE results, their subtraction from the CAD geometry L_0, the import of the new CAD model (unloaded geometry) into the FE tool, and the subsequent preprocessing (mesh generation and load application) and FE analysis.

For design optimization, a faster, non-iterative approach is desired to be directly integrated into the FE solver. A rather simple approach may be to reverse the load (pressure p_{SS} and p_{PS} on suction and pressure side as well as centrifugal load dF_C in Fig. 5b) and temperature conditions (ΔT). This is straight forward for the pressure loads ($-p_{SS}$) and ($-p_{PS}$), which are actually negligible as shown by Janke et al. (2016), and the temperature conditions ($-\Delta T$), see Fig. 5c. The only way to reverse the centrifugal load for a finite volume element dV is a negative material density ($-\rho$) which is applicable in Abaqus. Alternative sign changes of quantities r or dV would either be not applicable, change the model geometry, or distort other distributed loads. As airfoils are slender structures, reversing centrifugal loading may lead to nonlinear buckling instability which, however, can be suppressed by performing linear deformation analysis only. The discrepancy in the loaded geometry eigenfrequencies based on linear and nonlinear unloaded-geometry estimates is sufficiently small ($<$ 3Hz) for the first 10

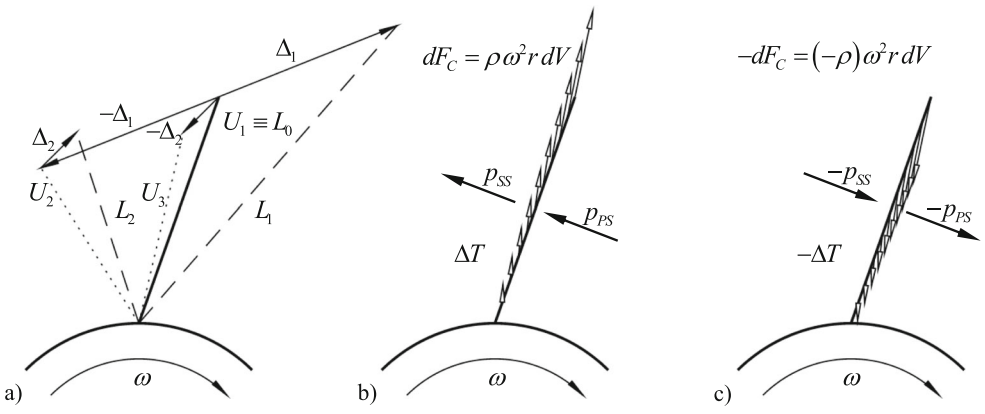

Fig. 5 Loaded-to-unloaded transformation: iterative approach **(a)** vs. reversing the actual loading **(b)** in the new approach **(c)**

eigenfrequencies of the first, last, and middle rotor of an industrial gas-turbine compressor as shown by black markers in Fig. 6. In contrast, the error is highly significant if no loaded-to-unloaded transformation is considered by applying loads and temperature conditions directly to the loaded geometry (white markers for loaded to additionally loaded≙L2L+). Also the maximal stress error being less than 2MPa is small compared to an error of about 80MPa without loaded-to-unloaded transformation. Since the geometry variation between the test rows is larger than variations to be expected during optimization of a specific row, the method may be regarded as reliable.

Contrary to the iterative approach, the suggested linear loaded-to-unloaded transformation can be directly implemented as a first calculation step in the FE analysis (displacement field has to be set as load free before proceeding with the further FE calculations) and requires only a negligible additional computational effort of less than 5s in our application. Thus, with the negative density, loaded-to-unloaded transformation becomes applicable to automated design optimization.

6 Optimization results of a test case

In order to improve the capabilities of automated design, the strategy proposed in this paper combines an efficient RSM-based multidisciplinary optimization process with direct loaded-to-unloaded transformation and a new strategy for assessing production tolerance to gain design robustness. Additionally, the automated identification of critical eigenmode shapes from Martin and Bestle (2018) is included to reduce the risk of high-cycle fatigue. All these methods now have to prove to deliver valid and efficient designs for a rather challenging test case driving optimization to its limits. To concentrate on the proposed approaches, the pre-blading part of the process in Fig. 1a is skipped and instead an existing airfoil design from an industrial gas turbine is chosen as initial design for the blading process. However, a much cheaper material (normal construction steel with comparatively low yield strength) is applied which causes violation of all structural constraints, whereas the design fulfills the aerodynamic ones. The design space is chosen rather restrictive where also human experts according to their experience would most likely feel comfortable with (degree of the splines is unlikely to deliver radically new design features). The ranges of the controls points in Fig. 3 are set to be ± 0.1 for $\tilde{r}$ and $\tilde{c}$, $\pm 2°$ for β_L and β_T, $\pm$2mm for t^{max}, $\pm$0.1mm for R_L and R_T, $\pm 10°$ for θ_S, $\pm$10mm for $\tilde{x}_S$, and ± 0.2 for $\tilde{\beta}$ and $\tilde{t}$. Initially higher ranges were tested, but did not lead to better designs, since optimal designs were located in a closer range about the initial design. Thus, it was decided to use tighter ranges for the sake of better design space exploration within the promising ranges.

Before analyzing the results, some details on the practical application of some of the introduced methods shall be given. First, the suggested approach for evaluating production tolerances requires the buildup of CAD models to obtain $S\left(\mathbf{p}_j^{\Delta}\right)$ (for each $\mathbf{p}_j^{\Delta} \in \mathcal{D}$ about each nominal design $\mathbf{p}^{nom}$) and the evaluation of the constraints $\mathbf{h}_i\left(\mathbf{p}_j^{\Delta}\right)$ (for each $\mathbf{p}_j^{\Delta} \in \mathcal{P}$). Since this may be computationally expensive, RSMs of the optimization process (Fig. 1) are utilized to assess the production tolerance which cuts down the computation time from days to a few hours for a single nominal design. This makes it applicable to at least a few selected nominal designs. Nonetheless, due to lack of computational resources (number of available CPUs and licenses), further reduction of the computational effort is required for complete evaluation of production tolerances during design optimization. This is achieved by avoiding generation of CAD model $S\left(\mathbf{p}_j^{\Delta}\right)$ for each sample $\mathbf{p}_j^{\Delta}$. Instead the spline distributions of the parameters $\mathbf{p}_j^{\Delta}$ are evaluated for intersections with $(p_i^{nom} \pm s_{\perp})$ in order to identify subset $\mathcal{P} \subset \mathcal{D}$. However, this is only possible for parameters p_i which are directly related to $\mathbf{s}_{\perp}$ and are decoupled from others, namely R_L, R_T, and t_{max}.

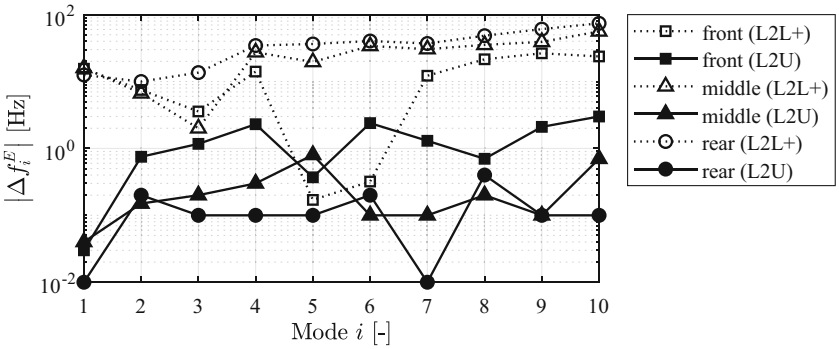

Fig. 6 Error of first 10 eigenfrequencies with linear loaded-to-unloaded transformation (L2U) and without (L2L+) for first, middle, and last rotor of an industrial gas turbine

Thus, only geometry changes symmetric to the camber line are considered at the current state. Because splines can be evaluated much faster than CAD models can be build up, the suggested production tolerance assessment becomes applicable to the optimization process (assessing 1000 nominal designs takes about 2–3 h).

For the probabilistic assessment of the objectives $P^{95}_{\Delta p_t}$ and $P^{95}_{\omega_{OD}}$ in (11), these design parameters are sampled within $\Delta p_i = 0.05$mm, which is a well achievable production tolerance for airfoil designs. The sampling size for all objectives in (11) is set to be 1000 using Latin-hypercube sampling (McKay et al. 1979), because in the present application the deviation of the calculated objectives based on 1000 samples compared to those based on 5000 samples is less than 3% and saves quite some time.

For mode shape specific tuning of eigenfrequency bands, the mode-resonance factor (5) has been introduced. In the present application, the first 15 eigenmodes of each design are evaluated in order to identify essential eigenmode shapes, namely 1B, 1T, 2B, 2T, 1C, 1H, 1S, 3T, 3B, 2H, 2C, where B denotes bending mode, T torsion mode, C chord-wise mode, H higher-order mode, S stiff-wise mode, and the number is related to the order of the respective mode. The associated penalty factors are $\mathbf{w}^E = [150, 140, 130, 120, 110, 100, 100, 100, 100, 100, 50]^T$. The engine orders N_j of interest are the first five engine orders, i.e., $N_j = 1, ..., 5$, with penalty factors $w^A_j = 100$, the number of airfoils installed on the next two upstream stators (rotors) penalized with $w^A_j = 100$, the number of airfoils installed on the next downstream stator (rotor) penalized with $w^A_j = 50$, and the difference between number of airfoils of the closest upstream and downstream stator (rotor) penalized with $w^A_j = 25$.

Tuning eigenmodes directly by considering each of the MRF_i as an individual objective or constraint, would harm the performance of the optimization algorithm. Therefore, all the constraints $h_i \leq 0$ in (11) (including all $MRF_i \leq 0$) are considered indirectly via a quadratic penalty strategy

$$C := \sum_i \frac{w_i}{s_i} \left(\max\{0, h_i\}\right)^2 \tag{12}$$

with weight factors w_i and scale factors s_i controlling the influence of constraint violations. During optimization the weights are scaled in such a way that, based on the last 100 design evaluations, the constraint h_i violated most times is assigned with $w_i := 2$, the one violated least times with $w_i := 1$, and all others accordingly in between. The scales s_i are calculated based on the DoE such that $\left(\max\{0, h_i\}\right)/s_i$ for each constraint h_i and all DoE samples equals one.

The weighted sum C is added to each objective, which causes the optimization algorithm not just to minimize theobjectives but also the degree of violation of the constraints. Thus, the optimization problem solved by the optimization algorithm reads as

$$\min_{\mathbf{p}^{nom} \in P} \begin{bmatrix} P^{95}_{\Delta p_t} + C \\ P^{95}_{\omega_{OD}} + C \\ \tilde{s}^{max}_{\perp} + C \end{bmatrix} \text{ s.t.}$$
$$P := \left\{ \mathbf{p}^{nom} \in \mathbb{R}^{N_P} \,|\breve{\mathbf{p}} \leq \mathbf{p}^{nom} \leq \hat{\mathbf{p}} \right\} . \tag{13}$$

The optimization of the compressor blade using a NSGA-II algorithm starts with an initial DoE of 3000 designs to feed the RSMs. Additionally about 2000 designs were evaluated during optimization to update the RSMs. Finally, none of the resulting designs is admissible, because either $s^{max}_{\perp} = 0$ in (10) or at least one $h_i > 0$ in (12). Obviously the design task is too challenging w.r.t. the chosen material to obtain a fully valid and producible design. However, lowering the expectation by allowing that a less critical eigenmode intersects with a higher engine order yielding values $MRF_i > 0$ in (5), and picking from these designs the one with the largest production tolerance being $s^{max}_{\perp} = 0.004$mm results in a design with appropriate aerodynamic turning and similar but slightly lower aerodynamic efficiency than the reference design. In conclusion, a human expert would now have to decide if the loss in aerodynamic efficiency is acceptable, or if the forced response of a less critical eigenmode harms the intended service life, or whether the challenging production tolerance negates the savings realized by the cheaper material.

A more detailed comparison of the structural dynamic characteristics between the reference and optimal design is given in Fig. 7 which shows essential eigenmode bands that have been identified together with others located among the essential ones. For the reference design, the Campbell diagram in Fig. 7a shows multiple intersections of engine orders (dashed-dotted lines) with eigenmode bands (brackets between dotted and solid lines) within the engine speed range (94–105%) where the intersections with 2C (2nd-order chord-wise bending mode), 1H/2H (1st and 2nd higher-order mode), and 3T (third torsion mode) are considered to be service life relevant. The optimization process is able to deliver a design with only one remaining intersection (3H) being less critical, Fig. 7b. Thus, the penalty strategy (12) and eigenmode classification procedure are able to drive optimization away from failure-critical force responses through the *MRF* criterion (5). On a first glance, this change in structural dynamic behavior

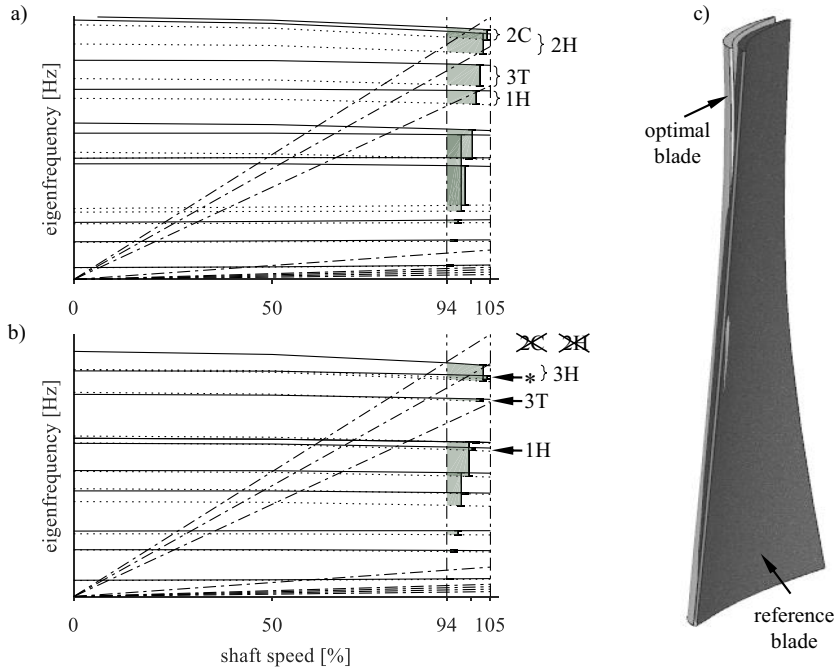

Fig. 7 Comparison of reference and optimal design in Campbell diagram for **a** reference and **b** optimal design, and **c** w.r.t. geometry (*unknown mode)

seems to result from an increased thickness and bow as shown in Fig. 7c. As a consequence, also the critical von Mises stress peaks at the airfoil surface as well as at the leading and trailing edges (Fig. 8a) are reduced to acceptable levels, as can be seen in Fig. 8b.

In order to better see the geometry changes, Fig. 9 shows the changes in the parameter distributions. The maximum thickness Δt^{max} in Fig. 9a is increased towards the root which is the main reason for the reduced stress level and elevated eigenfrequency bands. The changes ΔR_L, ΔR_T of the leading- and trailing-edge radii are negligible, hence, do not significantly contribute to the reduction of the stresses at leading and trailing edge. The increase of axial-shift $\Delta\tilde{x}_S$ and theta-shift $\Delta\theta_S$ (bow) may be driven by both structural as well as aerodynamic criteria, but the increased metal angles at the leading ($\Delta\beta_L > 0$) and trailing edge ($\Delta\beta_T > 0$) have certainly aerodynamic reasons. As $\Delta\beta_T$ is larger than $\Delta\beta_L$ to the most extent along $\tilde{r}$, the curvature of the blade has actually been decreased by the optimization. Because the optimal as well as the reference design fulfill the required aerodynamic turning, the reference design must already have suffered flow separation to a larger extent than the optimal design. The fact that both designs have similar aerodynamic efficiency means that the optimal design loses the potential gain in favor of structural integrity. A geometrical reason for the loss in gain might be the reduced $\tilde{\beta}$ and $\tilde{t}$ towards the leading edge, see Fig. 9b, c, whereas both remain nearly unchanged towards the trailing edge. The result is a higher shock wave compression for the optimal design.

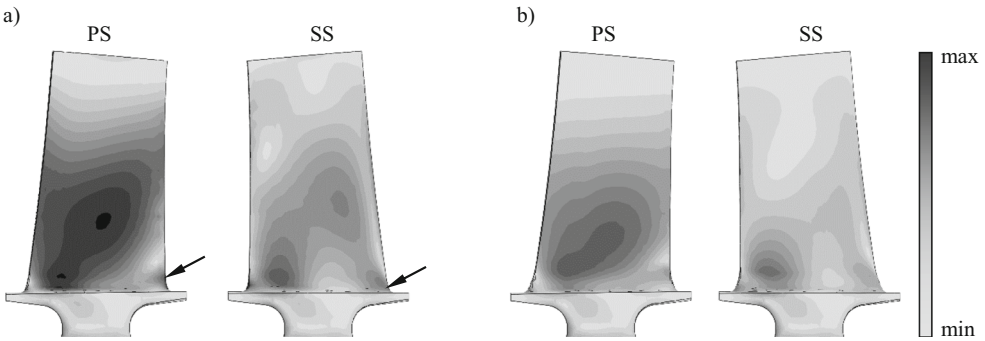

Fig. 8 Von Mises stress distributions of **a** reference design (black arrows mark critical stress peaks at leading and trailing edge) and **b** optimal design on pressure (PS) and suction (SS) side

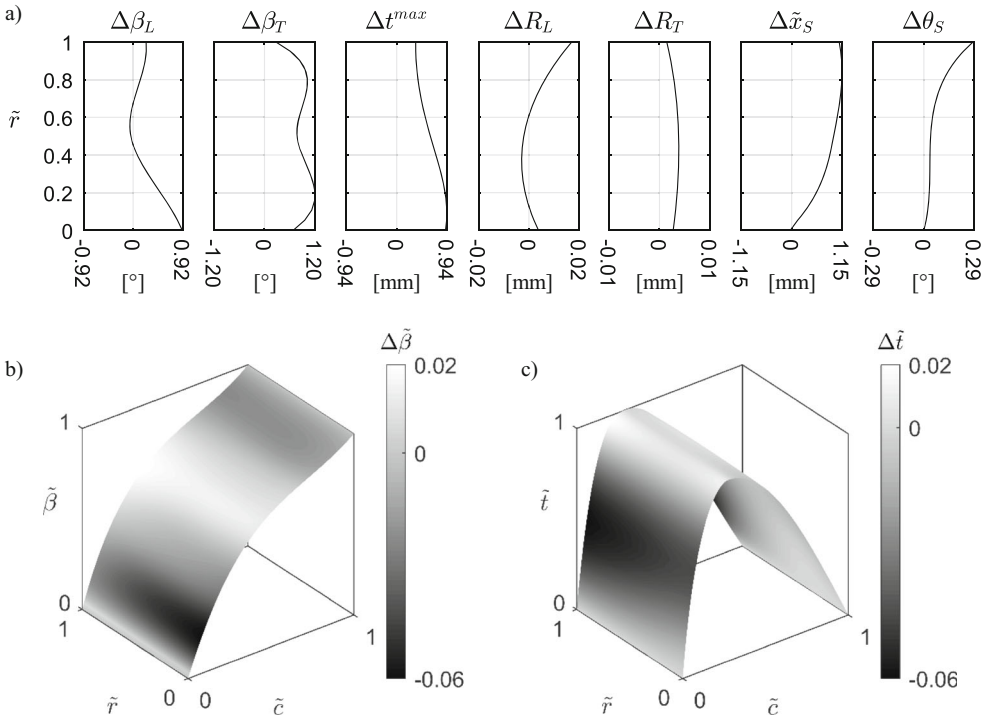

Fig. 9 Differences in geometry parameter distributions between the optimal robust design and the reference design for **a** one-dimensional distributions, **b** normalized chamber-line-angle distribution, and **c** normalized thickness distribution

7 Conclusions

The multidisciplinary optimization process proposed in this paper aims at performance improvement by diminution of shortcomings of existing processes with respect to efficient use of computing resources, quality of results, and robustness of the resulting designs. It introduces a flexible process structure based on discipline-specific RSMs to decouple different design evaluations from each other and from optimization. Thereby, an arbitrary number of instances may be executed in parallel to effectively use license and computer resources. As the process couples structural and aerodynamic design goals, consistency between both disciplines is ensured by permanent loaded-to-unloaded transformations of the airfoil geometry, where the proposed new and extremely fast strategy uses negative pressures, temperature changes, and density in order to reverse centrifugal loads. It is directly implemented in the FE analysis with little effort. Additionally, a method for automatically detecting failure-critical eigenmodes and associated uncertainty bands is incorporated to avoid high-cycle fatigue. In order to obtain optimization results with practical relevance for manufacturing, design robustness is addressed by determining a production tolerance which just ensures no violation of constraints. Application to a rather challenging design task demonstrates that the optimization process incorporating all the suggested methods is able to deliver results that reveal new opportunities for the design engineer to choose between design efficiency, service life, and manufacturing costs associated with production tolerances and type of blade material.

Acknowledgements The authors gratefully acknowledge AG Turbo and General Electric Switzerland for their support and permission to publish this paper. The responsibility for the content lies solely with its authors.

Funding information The research was conducted as part of the joint research program COOREFLEX-turbo in the frame of AG Turbo. The work was financially supported by the Bundesministerium für Wirtschaft und Technologie (BMWi) as per resolution of the German Federal Parliament under grant number 03ET7021J.

References

Astrua P, Piola S, Silingardi A, Bonzani F (2012) Multi-objective constrained aero-mechanical optimization of an axial compressor transonic blade. In: Proceedings of ASME Turbo Expo 2012, Copenhagen, Denmark, pp GT2012–68993

Blocher M, Fernández IEG (2014) Time-linearized forced response analysis of a counter rotating fan; Part I: Theoretical concept of a fully Time-Linear forced response analysis. In: Proceedings of ASME Turbo Expo 2014, Düsseldorf, Germany, pp GT2014–25833

Buske C, Krumme A, Schmidt T, Dresbach C, Zur S, Tiefers R (2016) (2016) Distributed multidisciplinary optimization of a turbine blade regarding performance, reliability and castability. In: Proceedings of ASME Turbo Expo 2016, Seoul, pp GT2016–56079

Cumpsty N (2004) Compressor aerodynamics. Krieger Publishing Company, Malabar

Diener OHF, von Backström TW, van der Spuy SJ, Hildebrandt T (2016) Multi-Disciplinary optimization of a mixed-flow compressor impeller. In: Proceedings of ASME Turbo Expo 2016, Seoul, pp GT2016–57008

Dow EA, Wang Q (2015) The implications of tolerance optimization on compressor blade design. ASME J Turbomach 137(10):101008-101008-7. https://doi.org/10.1115/1.4030791

Du X, Sudjianto A, Chen W (2004) An integrated framework for optimization under uncertainty using inverse reliability strategy. J Mech Des 126:562–570

Dutta AK (2011) An automated multi-objective optimization approach for aerodynamic compressor blade designs. Shaker, Germany

Flassig PM, Dutta AK, Bestle D (2008) Robuste Auslegung von Verdichterschaufeln. In: Proceedings of Deutscher Luft- und Raumfahrtkongress, Darmstadt, Germany, DLRK, pp 2008–08117

Flassig PM (2011) Unterstützende Optimierungsstrategien zur robusten aerodynamischen Verdichterschaufelauslegung. Shaker, Germany

Goerke D, Le Denmat AL, Schmidt T, kocian F, Nicke E (2012) Aerodynamic and mechanical optimization of CF/PEEK blades of a counter rotating fan. In: Proceedings of ASME Turbo Expo 2012, Copenhagen, Denmark, pp GT2012–68797

Hartwig L, Bestle D (2016) Enhancing low-fidelity compressor design by utilizing a surrogate model based on higher-fidelity information. In: Proceedings of 7th IC-SCCE, Athens, Greece

Hartwig L, Bestle D (2017) Compressor blade design for stationary gas turbines using dimension reduced surrogate modeling. In: IEEE Congress on evolutionary computation (CEC), san Sebastián, Spain, pp e–17366

Hecker P, Delimar D, Brandl H, Lötzerich M. (2011) Process integration and automated numerical design optimization of an eigenfrequency analysis of a compressor blade. In: Proceedings of ASME Turbo Expo 2011, Vancouver, Canada, pp GT2011–4548

Janke C, Goller M, Martin I, Gaun L, Bestle D (2016) 3D CFD compressor map computation of a multi-atage axial compressor with off-design adjusted rotor geometries. In: Proceedings of ASME Turbo Expo 2016, Seoul, South Korea, pp GT2016–56745

Joly MM, Verstraete T, Panlagua G (2014) Multidisciplinary design optimization of a compact highly loaded fan. Struct Multidiscip Optim 49:471–483

Keskin A (2007) Process integration and automated multi-objective optimization supporting aerodynamic compressor design, shaker, aachen

Martin I, Bestle D (2016) Automated mode identification of airfoil geometries to be used in an optimization process. In: Proceedings of ASME Turbo Expo 2016, Seoul, South Korea, pp GT2016–56987

Martin I, Bestle D (2018) Automated eigenmode classification for airfoils in the presence of fixation uncertainties. Eng Appl Artif Intell 2018 67:187–196

McKay MD, Beckman RJ, Conover WJ (1979) A comparison of three methods for selecting values of input variables in the analysis of output from a computer code. Technometrics 21:239–245

Motta RdS, Afonso SMB (2016) An efficient procedure for structural reliability-based robust design optimization. Struct Multidiscip Optim 54:511–530

Nicholas T (2006) High cycle fatigue: a mechanics of materials perspective. Elsevier Science, Amsterdam

Pierret S, Coelho RF, Kato H (2007) Multidisciplinary and multiple operating points shape optimization of three-dimensional compressor blades. Struct Multidiscip Optim 33:61–70

Pöhlmann F, Bestle D (2012) Multi-objective compressor design optimization using multi-design transfer between codes of different fidelity. In: Proceedings of ASME Turbo Expo 2012, Copenhagen, Denmark, pp GT2012–68577

Rühle T, Bestle D (2010) Compressor design and optimisation based on throughflow calculation. In: Proceedings of ADOS Automatic Design Optimization Seminar 2010, Derby, UK

Schörner R, Bestle D (2012) Coupled optimization of compressor blade roots and rotor grooves for industrial gas-turbines. In: Proceedings of 5th IC-SCCE International Conference: From Scientific Computing to Computational Engineering, Athens, Greece

Strouhal V (1878) ÜBer eine besondere Art der Tonerregung. Ann Phys Chem 5:216–251

Wu CH (1952) General theory of three-dimensional flow in subsonic and supersonic turbomachines of axial-, radial-, and mixed-flow types. NACA Report TN-2604, NASA, Cleveland USA